New understanding of nuclei spectra properties observed by the AMS-02 experiment

Xu-Lin Dong

College of Physics, Hebei Normal University, No. 20 Road East 2nd Ring South, Shijiazhuang, 050024 Hebei, China and Key Laboratory of Particle Astrophysics, Institute of High Energy Physics, Chinese Academy of Sciences, No. 19 B Yuquan Road, Shijingshan District, Beijing, 100049 Beijing, China

Yu-Hua Yao[*]

College of Physics, Chongqing University, No. 55 Daxuecheng South Road, High-tech District, Chongqing 401331, China and Key Laboratory of Particle Astrophysics, Institute of High Energy Physics, Chinese Academy of Sciences, No. 19 B Yuquan Road, Shijingshan District, Beijing, 100049 Beijing, China

Yi-Qing Guo[†]

Key Laboratory of Particle Astrophysics, Institute of High Energy Physics, Chinese Academy of Sciences, No. 19 B Yuquan Road, Shijingshan District, Beijing, 100049 Beijing, China and College of Physics, University of Chinese Academy of Sciences, No. 19 A Yuquan Road, Shijingshan District, Beijing, 100049 Beijing, China

Shu-Wang Cui[‡]

College of Physics, Hebei Normal University, No. 20 Road East 2nd Ring South, Shijiazhuang, 050024 Hebei, China

(Received 13 December 2023; accepted 21 February 2024; published 21 March 2024; corrected 4 April 2024)

The AMS-02 experiment has observed new properties of primary cosmic rays (CRs) categorized into two groups: He-C-O-Fe and Ne-Mg-Si-S, which are independent of CR propagation. In this study, we investigate the unexpected properties of these nuclei using a spatial propagation model. All nuclei spectra are accurately reproduced and separated into primary and secondary contributions. Our findings include: 1. Primary CR spectra are identical. 2. Our calculations align with AMS-02 results for primary-dominated nuclei within a 10% difference, but show significant discrepancies for the secondary-dominated nuclei. 3. The primary element abundance at around 200 GeV is presented and compared with previous solar and Galactic results. We hope that future DAMPE experiments can provide more experimental observational evidence to validate our model calculations.

DOI: 10.1103/PhysRevD.109.063027

I. INTRODUCTION

The discovery of cosmic rays (CR) has spanned over a hundred years, yet their origin, acceleration, and propagation remain ambiguous. Primary CR nuclei are generally believed to be accelerated by astrophysical sources, such as supernova remnants [1], or pulsars [2]. Secondary CRs are produced through spallation reactions taking place at the production site or in the interstellar medium on their way to Earth. The CR spectrum and chemical composition, for both primaries and secondaries, provide the most important clues to cosmic-ray origin and propagation [3,4]. They can trace effects within CR sources by probing the average CR residence time and gas density inside accelerating sites, and can also trace a change in the diffusion coefficient between the Galactic disc and halo. Elemental abundance can also give essential clues to the acceleration sites and timescales.

The latest generation of experiments is currently delving into the intricate details of CR phenomenology. An observed and confirmed hardening from the uniform power-law of the CR spectrum for all elements around a rigidity of a few hundred GeV has sparked significant interest [5–12]. Various models, primarily categorized as sources [13], propagation [14–16], and reacceleration [17,18], have been proposed to provide explanations. Simultaneously addressing the

[*]yaoyh@cqu.edu.cn
[†]guoyq@ihep.ac.cn
[‡]cuisw@hebtu.edu.cn

measured positron excess [19] and the diffuse gamma-ray hardening in the Galactic disk [20], the propagation effects with a nearby source are strongly favored [21,22]. In the case of a nearby source, it is likely that all the indices of primary components are identical, particularly when the energy is higher than several hundred GeV, as the interactions during transportation mainly affect the spectra of lower energy.

The precise measurements and large statistics provided by AMS-02 have unveiled new properties in the nuclei spectra. The primary and secondary components for heavy nuclei from carbon to iron fluxes are estimated by performing fit to the weighted sum of the flux of primary CR oxygen (silicon) and the flux of secondary CR flux boron (fluorine) [10,11,23]. It calibrate their abundance of primary and secondary components independently from models, revealing that primary He-C-O-Fe are distantly different from Ne-Mg-Si-S and there are at least two classes of secondary components [10,23–26]. The study by [27] investigated the consistency of injected spectra among different groups of nuclei, assuming spatially uniform propagation, indicating intrinsic differences in the injection spectra.

In this study, we have utilized the spatially dependent propagation model [21,22], which was extended and developed based on the two-halo propagation model proposed by [14], to examine the relative contributions of primary and secondary components in each nuclei spectrum. The structure of this paper is organized as follows: we initially introduce the spatially dependent propagation model, followed by the presentation of the results pertaining to each nucleon spectrum and the corresponding abundance outcomes, and ultimately, we provide our concluding remarks.

II. METHODOLOGY

In this section, we describe the propagation setup that will be used throughout the paper, which is based on the model settings presented in [21,22]. CR dynamics in the Galaxy is generally described by a differential equation [28–31] that includes acceleration, loss, and transport terms, described as

$$\frac{\partial \psi}{\partial t} = Q(\mathbf{r}, p) + \nabla \cdot (D_{xx}\nabla\psi - \mathbf{V}_c\psi) + \frac{\partial}{\partial p} p^2 D_{pp} \frac{\partial}{\partial p} \frac{1}{p^2}\psi - \frac{\partial}{\partial p}\left[\dot{p}\psi - \frac{p}{3}(\nabla \cdot \mathbf{V}_c\psi)\right] - \frac{\psi}{\tau_f} - \frac{\psi}{\tau_r} \quad (1)$$

where $Q(\mathbf{r}, p)$ is the source function, D_{xx} and D_{pp} are the spatial diffusion coefficient and diffusion coefficient in the momentum-space, respectively. $\mathbf{V}_c$ is the convection velocity, τ_f and τ_r are the characteristic timescales used to describe the fragmentation and radioactive decay.

Spatially dependent diffusion is considered with source-calibrating diffuse coefficient, which is further support by the observation of slow diffusion region around the source [32,33]. Both CR sources and interstellar medium chiefly spread within the Galactic disk, causing a much slower propagation process close to the Galactic disk ($|z| \leq \xi z_0$). While regions far way from the disk ($|z| > \xi z_0$) particles transport as the traditional assumption. The spatial distribution of CR sources [34] is parametrized as

$$f(r,z) = \left(\frac{r}{r_\odot}\right)^{1.25} \exp\left[-\frac{3.87(r-r_\odot)}{r_\odot}\right] \exp\left(-\frac{|z|}{z_s}\right), \quad (2)$$

where $r_\odot = 8.5$ kpc and $z_s = 0.2$ kpc.

The propagation coefficient is anticorrelated with the source density and is described as

$$D_{xx}(r, z, \mathcal{R}) = D_0 F(r,z) \beta^\eta \left(\frac{\mathcal{R}}{\mathcal{R}_0}\right)^{\delta_0 F(r,z)}, \quad (3)$$

where the function $F(r, z)$ is defined as:

$$F(r,z) = \begin{cases} g(r,z) + [1 - g(r,z)]\left(\frac{z}{\xi z_0}\right)^n, & |z| \leq \xi z_0 \\ 1, & |z| > \xi z_0 \end{cases}, \quad (4)$$

with $g(r, z) = N_m/[1 + f(r, z)]$. The distributions of F(r, z) with respect to the radial distance r and vertical height z could be referenced from the work in [22].

The injection spectrum of sources is assumed to be a broken power-law form, whose power indexes and flux normalization factors are listed in Table I.

CR species spectra is obtained by extending DRAGON [31] to solve the general diffusion-loss transport equation. The corresponding transport parameters are given in Table II. The force-field approximation [35] is adopted to for solar modulation effect.

TABLE I. Spectral injection parameters and solar modulation energy for each element.

Element	Normalization [GeV^{-1} m^{-2} s^{-1} sr^{-1}]	ν_2[a]	Abundance	E_{modu} [GeV/nucleon]
H	4.35×10^{-2}	2.45	9.41×10^5	0.85
He	2.54×10^{-3}	2.36	55000	0.75
C	9.48×10^{-5}	2.38	2050	0.7
N	5.09×10^{-6}	2.38	110	0.7
O	1.29×10^{-4}	2.40	2800	0.6
Ne	1.74×10^{-5}	2.41	377	0.55
Na	2.31×10^{-7}	2.41	5	0.75
Mg	2.31×10^{-5}	2.41	500	0.6
Al	1.99×10^{-6}	2.41	43	0.45
Si	2.43×10^{-5}	2.42	525	0.65
S	3.93×10^{-6}	2.42	85	0.6
Fe	2.59×10^{-5}	2.43	560	0.8

[a]$\nu_1 = 2.3, \mathcal{R}_{br} = 6$ GeV.

TABLE II. Parameters for the SDP propagation model.

D_0[a] [cm^{-2} s^{-1}]	δ_0	N_m	ξ	n	v_A [km s^{-1}]	z_0 [kpc]
5×10^{28}	0.58	0.24	0.082	4.0	6	5

[a]Reference rigidity is 4 GV.

III. RESULTS

The propagated spectra of nuclei (ranging from helium to iron), including their primary and secondary components, are presented as functions of per nucleon kinetic energy. Firstly the boron and fluorine flux are presented in Fig. 1, which are thought purely secondary CRs produced by primary ones during their journal to the Earth. It can be seen that the model-calculated ratios are consistent with the observational data from experiments.

Oxygen and silicon fluxes are given in Fig. 2, as well as their primary, secondary contributions. The primary component represents the injection part and the secondary one mainly stems from the fragmentation of heavier elements. The lower panel of figures illustrate the partitioning of the primary component in relation to the total proton, as a function of energy. It is evident that oxygen is predominantly dominated by the primary component, whereas a relatively small portion (approximately 10%) at the energy of 10 GeV of the silicon spectra originates from secondary production. The silicon fluxes show a decreasing secondary component and an increasing primary component with increasing energy. In the study of AMS abundance ratios at the source [23], the oxygen and silicon fluxes are considered to be purely contributed by primary CRs. However, our study reveals that the silicon flux is not as purely primary as that of oxygen.

Figure 3 demonstrates fluxes of primary, secondary, and total flux of helium, carbon, as well as the previously claimed distinct classes nickel, magnesium, and sulfur,

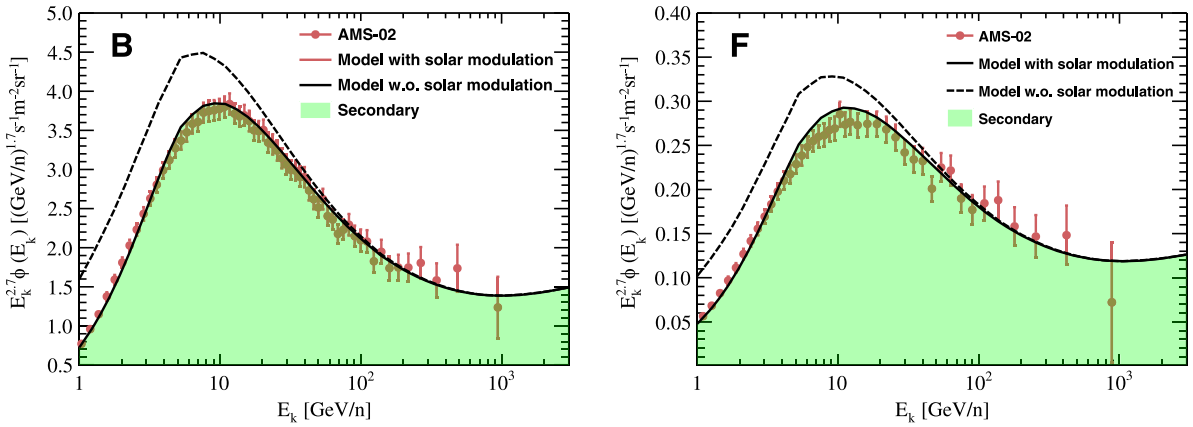

FIG. 1. Fluorine and boron CRs, with AMS-02 measurements [9,26].

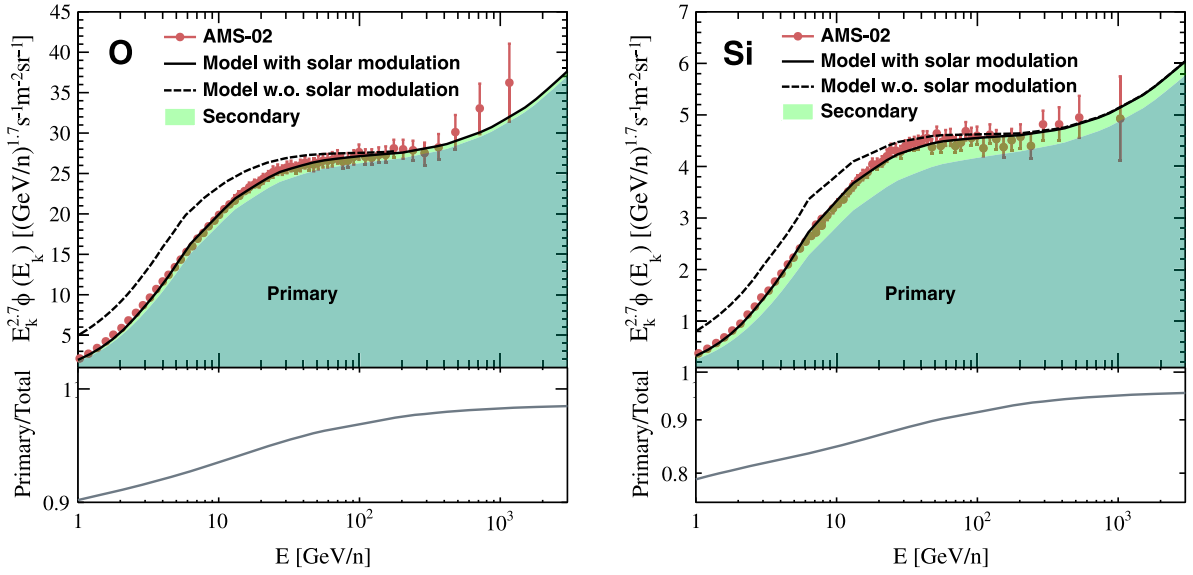

FIG. 2. Left: The oxygen flux, compared with data from [36]. Right: silicon flux, compare with data from [10]. The primary and secondary component contributions are shown by the dark green and light green shading, respectively. The lower panel of each figure presents the primary-to-total flux ratios.

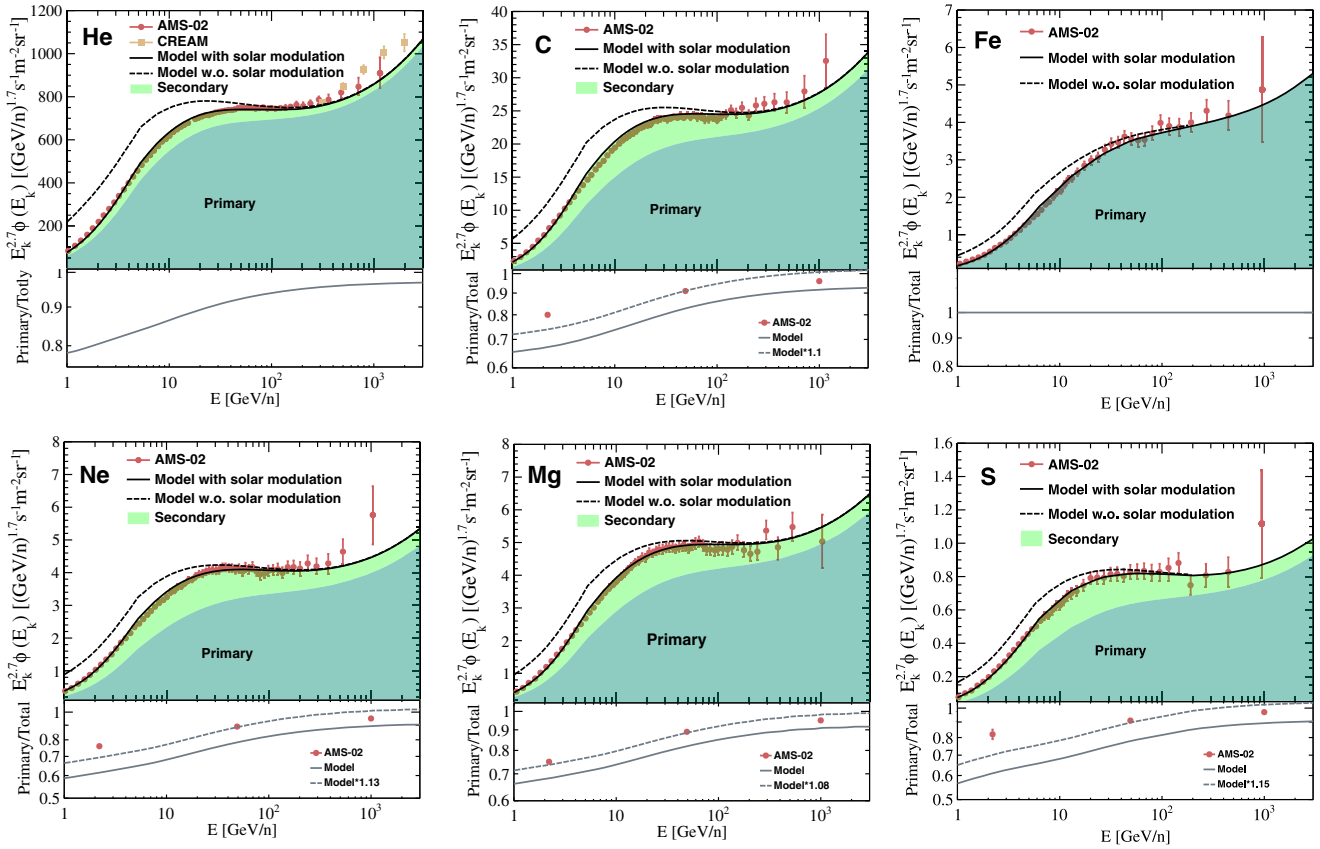

FIG. 3. From top to bottom, and from left to right, they are helium, carbon, iron, nickel, magnesium, and sulfur, with AMS-02 measurements [10,11,23,36,37]. The primary and secondary component contributions are shown by the dark green and light green shading, respectively. The lower panel of each figure presents the primary-to-total flux ratios, compared with ratios from [23].

revealing that all their primary-to-total flux ratios are similar to each other. Additionally, the solid and dashed lines in the lower panel of each figure represent our model-calculated ratios and our model-calculated ratios times a factor to match the AMS abundance ratios at the source [23], respectively. It is evident that out model-calculated ratios are all lower than those based on experimental data, and the reason for this is that the observed silicon flux contains not negligible secondaries.

The nitrogen, sodium, and aluminum fluxes are displayed from left to right in Fig. 4. These ratios are notably distinct from those shown in Fig. 3 due to their substantial secondary components. Additionally, the primary-to-total flux ratios in the lower panel of each figure indicate significant

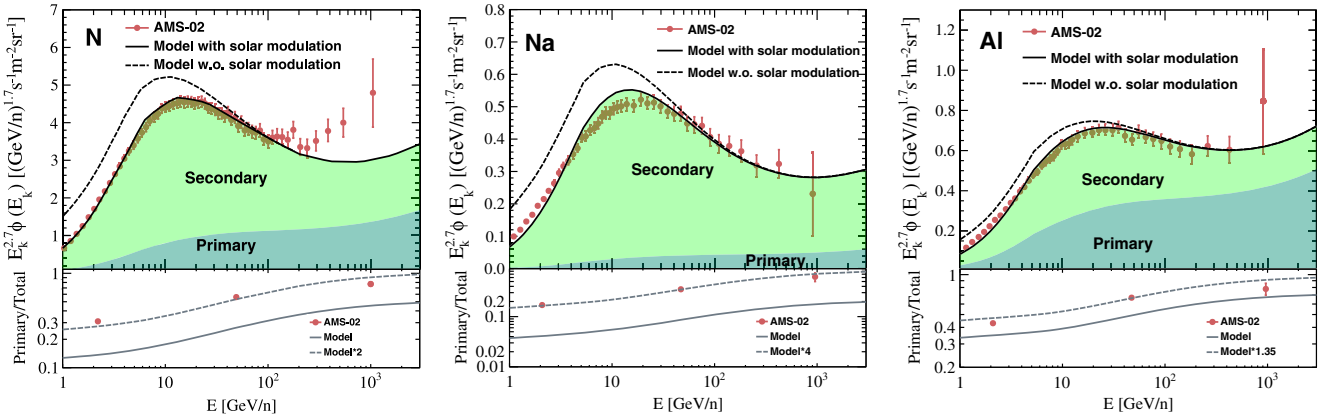

FIG. 4. From left to right, they are: nitrogen, sodium, aluminum, with the data from [25]. The lower panel of each figure presents the primary-to-total flux ratios, compared with ratios from [25].

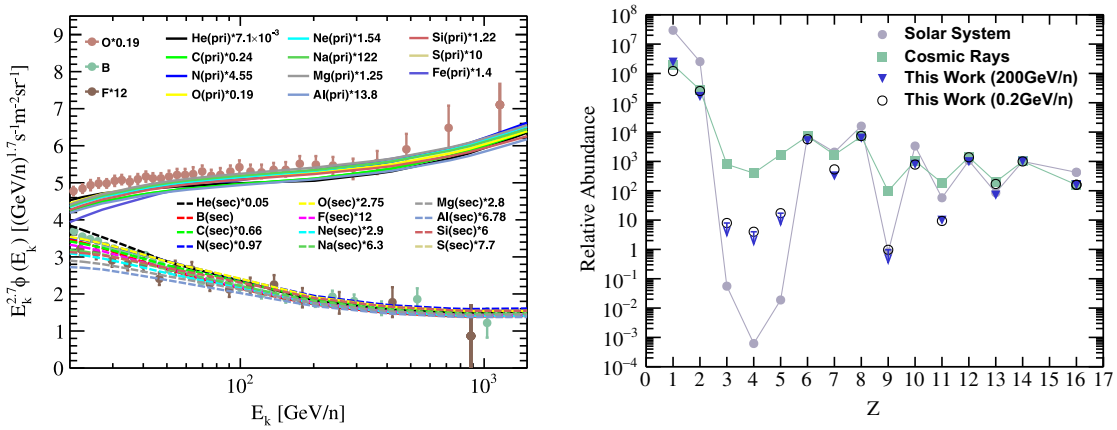

FIG. 5. Left: the fluxes of cosmic nuclei from primary and secondary contributions. For display purposes only, the fluxes were rescaled as indicated. Given that fluorine and boron cosmic rays in Fig. 1 are purely secondary, and oxygen is almost primary in Fig. 2, the model results are compared with AMS-02 observed fluxes [9,26,36] here as well. Right: relative abundances of high-energy (200 GeV/nucleon) cosmic rays, compared to the low-energy (0.2 GeV/nucleon) cosmic rays and the present-day solar system, which from [38]. Abundances are normalized to Si $= 10^3$.

differences between our calculations and results based on observational secondary and primary components. This suggests that there may be a greater secondary contribution to the spectra of these secondary-dominated nuclei than previously estimated [25].

The left panel of Fig. 5 displays the primary and secondary components of nuclei from helium to iron. The fluxes are rescaled as indicated for display purposes only. It can be observed that all primary components are mostly the same, which is also evident from the injected spectral index listed in Table I. However, there are marginal differences between the secondary components in the lower energy range, mainly due to the cross-section differences in secondary production. The right panel of Fig. 5 presents the relative abundances of high-energy (200 GeV/nucleon) cosmic rays, normalized to Si $= 10^3$ and compared to the low-energy (0.2 GeV/nucleon) cosmic rays and the present-day solar system from [38]. It is evident that there are significant differences for each element compared to those in the solar system, especially for the Z-odd ones.

Here we investigate the spectra of different nuclei primarily based on the AMS-02 data, as the target energy range in this study exceeds tens of GeV, where it is free from solar modulation. The model calculations compared with measurements for each nucleus at low energies outside the solar system by Voyager-1 [39] are presented in the Appendix. It is evident that there are significant deviations between the model calculations without solar modulation and Voyager's observations. The origin of this discrepancy may be due to Voyager still being within the influence of the solar magnetic field, or it could be attributed to the accuracy of solar modulation in this work. These two aspects will be addressed in our future work, although they do not impact the conclusions drawn in this paper.

IV. SUMMARY

This work is aimed at understanding the primary and secondary components of each CR species recently observed by AMS. We took advantage of SDP propagation model, tracing the spectra from originate from sources and production during the transportation. We found that boron and fluorine are purely secondaries while the silicon spectra is not as pure primary as the oxygen. The primary component of CR species (He-C-O-Ne-Mg-Si-S-Fe) are the same class, N-Na-Al are secondary-dominated. All primary component are increasing with energy. When particle energies are above TeV, diffuse propagation dominates and particle interaction is negligible. If they were one group, they would stay together with higher energy. Future more precise measurements above TeV could test if there are significant spectral differences and validate our model calculations. The primary abundance of CR nuclei presented differs from that of the solar system. This clean dataset of primary and secondary component could help us to check the consistency between the observed data and the CR model.

ACKNOWLEDGMENTS

This work is supported by the National Natural Science Foundation of China (No. 12275279, No. 12373105, No. 12320101005) and the China Postdoctoral Science Foundation (No. 2023M730423).

APPENDIX: COMPARISON BETWEEN MODEL DATA AND THE LOCAL INTERSTELLAR OBSERVATIONS

The model calculations extended to MeV per nucleon, compared with measurements for each nucleus at low energies outside the solar system by Voyager-1 [39], are presented in Figs. 6,7, and 8.

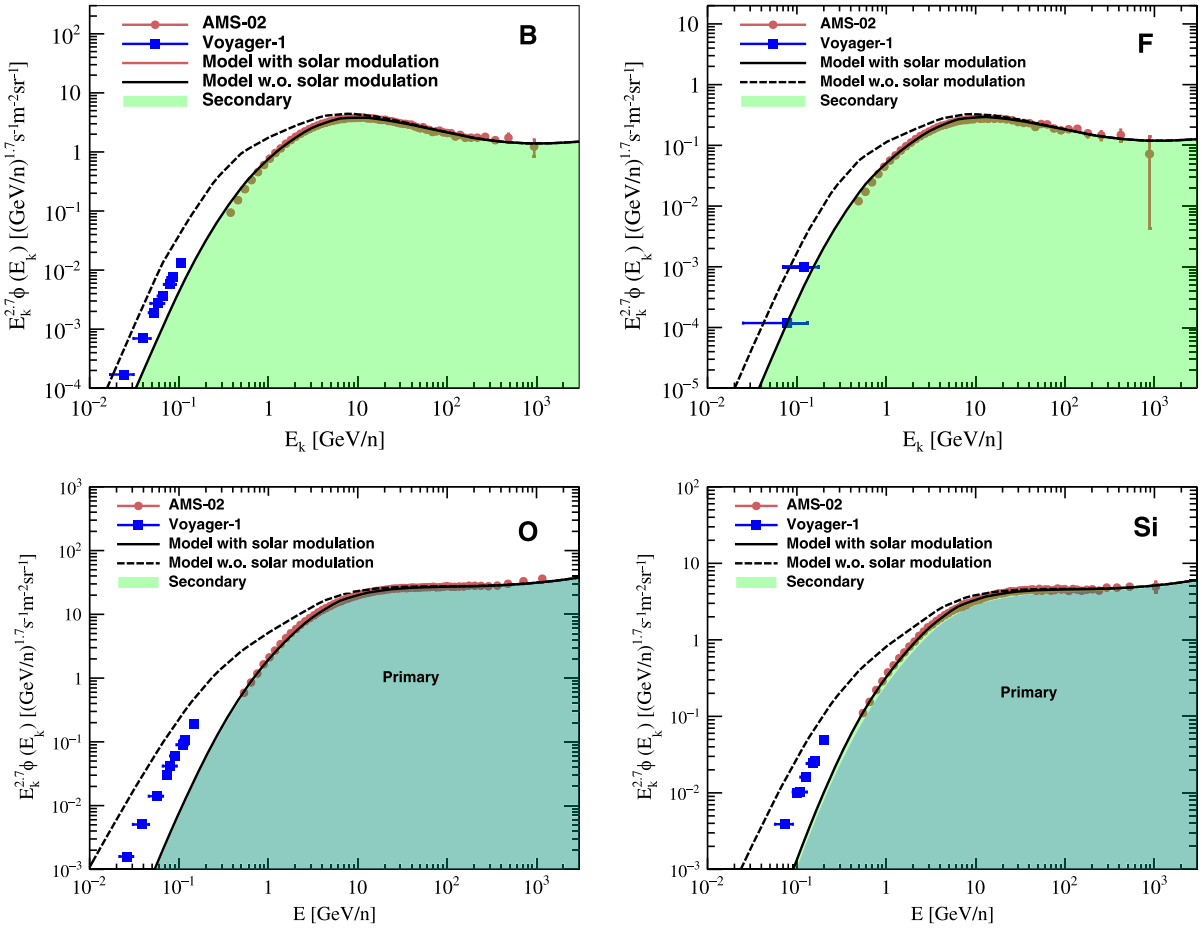

FIG. 6. Fluorine, boron, oxygen, and silicon CRs, with AMS-02 [9,10,26,36] and the Voyager-1 [39] observations. The model data in this figure is the same as in Fig. 1 and Fig. 2, except that in this figure, the low-energy range is extended to tens of MeV per nucleon for comparison with Voyager's observations.

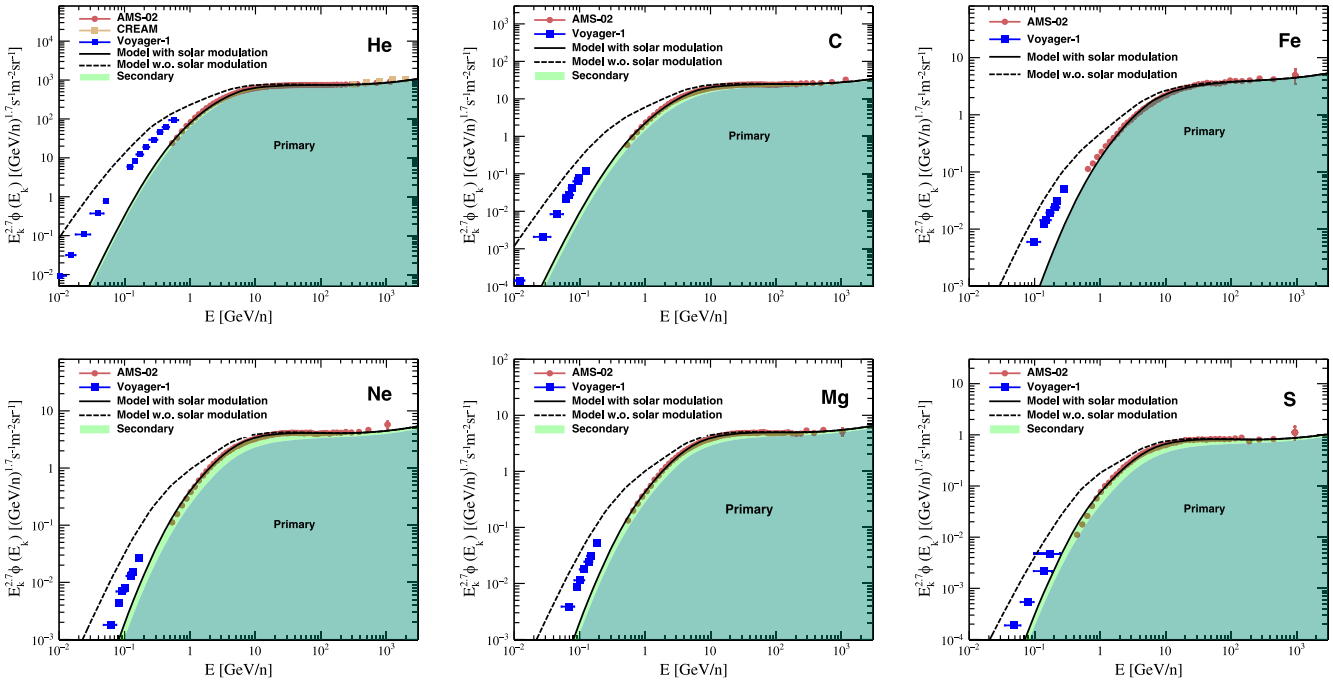

FIG. 7. From top to bottom, and from left to right, they are helium, carbon, iron, nickel, magnesium, and sulfur, with AMS-02 [10,11,23,36,37] and Voyager-1 [39] observations. The model data in this figure is the same as in Fig. 3, except that in this figure, the low-energy range is extended to tens of MeV per nucleon for comparison with Voyager's observations.

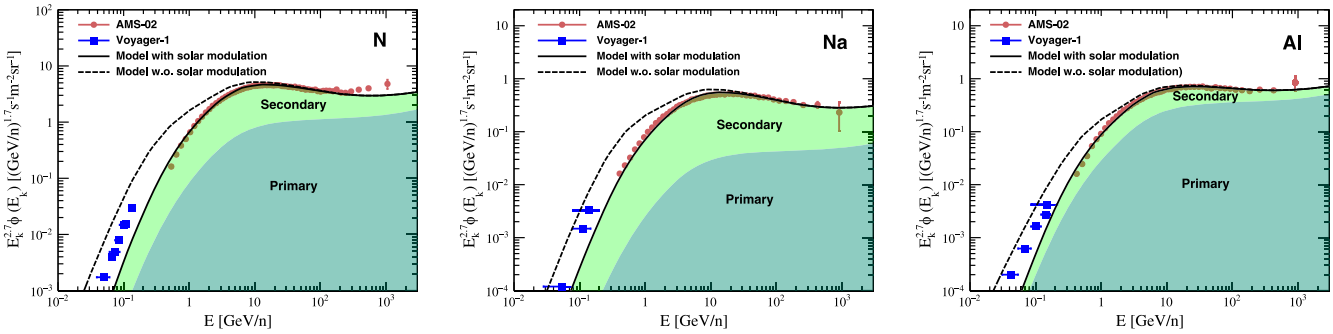

FIG. 8. From left to right, they are: nitrogen, sodium, aluminum, with the data from AMS-02 [25] and Voyager-1 [39] observations. The model data in this figure is the same as in Fig. 4, except that in this figure, the low-energy range is extended to tens of MeV per nucleon for comparison with Voyager's observations.

[1] W. Baade and F. Zwicky, On Super-Novae, Proc. Natl. Acad. Sci. U.S.A. **20**, 254 (1934).
[2] Olivia Meredith Bitter and Dan Hooper, Constraining the local pulsar population with the cosmic-ray positron fraction, J. Cosmol. Astropart. Phys. 10 (2022) 081.
[3] Isabelle A. Grenier, John H. Black, and Andrew W. Strong, The nine lives of cosmic rays in galaxies, Annu. Rev. Astron. Astrophys. **53**, 199 (2015).
[4] Richard E. Lingenfelter, The origin of cosmic rays: How their composition defines their sources and sites and the processes of their mixing, injection, and acceleration, Astrophys. J. Suppl. Ser. **245**, 30 (2019).
[5] A. D. Panov, J. H. Adams, H. S. Ahn *et al.*, Energy spectra of abundant nuclei of primary cosmic rays from the data of ATIC-2 experiment: Final results, Bull. Russ. Acad. Sci., Phys. **73**, 564 (2009).
[6] O. Adriani, G. C. Barbarino, G. A. Bazilevskaya *et al.*, PAMELA measurements of cosmic-ray proton and helium spectra, Science **332**, 69 (2011).
[7] Y. S. Yoon, H. S. Ahn, P. S. Allison *et al.*, Cosmic-ray proton and helium spectra from the first CREAM flight, Astrophys. J. **728**, 122 (2011).
[8] Q. An, R. Asfandiyarov, P. Azzarello *et al.*, Measurement of the cosmic ray proton spectrum from 40 GeV to

100 TeV with the DAMPE satellite, Sci. Adv. **5**, eaax3793 (2019).
[9] M. Aguilar, L. Ali Cavasonza, G. Ambrosi *et al.*, Observation of new properties of secondary cosmic rays lithium, beryllium, and boron by the alpha magnetic spectrometer on the International Space Station, Phys. Rev. Lett. **120**, 021101 (2018).
[10] M. Aguilar, L. Ali Cavasonza, G. Ambrosi *et al.*, Properties of neon, magnesium, and silicon primary cosmic rays results from the alpha magnetic spectrometer, Phys. Rev. Lett. **124**, 211102 (2020).
[11] M. Aguilar, L. Ali Cavasonza, M. S. Allen *et al.*, Properties of iron primary cosmic rays: Results from the alpha magnetic spectrometer, Phys. Rev. Lett. **126**, 041104 (2021).
[12] M. Aguilar, L. Ali Cavasonza, G. Ambrosi *et al.*, The Alpha Magnetic Spectrometer (AMS) on the International Space Station: Part II—Results from the first seven years, Phys. Rep. **894**, 1 (2021).
[13] S. Thoudam and J. R. Hörandel, Nearby supernova remnants and the cosmic ray spectral hardening at high energies, Mon. Not. R. Astron. Soc. **421**, 1209 (2012).
[14] N. Tomassetti, Origin of the cosmic-ray spectral hardening, Astrophys. J. Lett. **752**, L13 (2012).
[15] Daniele Gaggero, Alfredo Urbano, Mauro Valli, and Piero Ullio, Gamma-ray sky points to radial gradients in cosmic-ray transport, Phys. Rev. D **91**, 083012 (2015).
[16] C. Jin, Y.-Q. Guo, and H.-B. Hu, Spatial dependent diffusion of cosmic rays and the excess of primary electrons derived from high precision measurements by AMS-02, Chin. Phys. C **40**, 015101 (2016).
[17] P. L. Biermann, J. K. Becker, J. Dreyer, A. Meli, E.-S. Seo, and T. Stanev, The origin of cosmic rays: Explosions of massive stars with magnetic winds and their supernova mechanism, Astrophys. J. **725**, 184 (2010).
[18] S. Thoudam and J. R. Hörandel, GeV–TeV cosmic-ray spectral anomaly as due to reacceleration by weak shocks in the galaxy, Astron. Astrophys. **567**, A33 (2014).
[19] M. Aguilar, L. Ali Cavasonza, G. Ambrosi *et al.*, Towards understanding the origin of cosmic-ray positrons, Phys. Rev. Lett. **122**, 041102 (2019).
[20] M. Ackermann, M. Ajello, W. B. Atwood *et al.*, Fermi-LAT observations of the diffuse γ-ray emission: Implications for cosmic rays and the interstellar medium, Astrophys. J. **750**, 3 (2012).
[21] Yi-Qing Guo, Zhen Tian, and Chao Jin, Spatial-dependent propagation of cosmic rays results in the spectrum of proton, ratios of P/P, and B/C, and anisotropy of nuclei, Astrophys. J. **819**, 54 (2016).
[22] Yi-Qing Guo and Qiang Yuan, Understanding the spectral hardenings and radial distribution of Galactic cosmic rays and Fermi diffuse γ rays with spatially-dependent propagation, Phys. Rev. D **97**, 063008 (2018).
[23] M. Aguilar, L. Ali Cavasonza, B. Alpat *et al.*, Properties of cosmic-ray sulfur and determination of the composition of primary cosmic-ray carbon, neon, magnesium, and sulfur: Ten-year results from the alpha magnetic spectrometer, Phys. Rev. Lett. **130**, 211002 (2023).
[24] M. Aguilar, L. Ali Cavasonza, B. Alpat *et al.*, Precision measurement of cosmic-ray nitrogen and its primary and secondary components with the alpha magnetic spectrometer on the International Space Station, Phys. Rev. Lett. **121**, 051103 (2018).
[25] M. Aguilar, L. Ali Cavasonza, B. Alpat *et al.*, Properties of a new group of cosmic nuclei: Results from the alpha magnetic spectrometer on sodium, aluminum, and nitrogen, Phys. Rev. Lett. **127**, 021101 (2021).
[26] M. Aguilar, L. Ali Cavasonza, M. S. Allen *et al.*, Properties of heavy secondary fluorine cosmic rays: Results from the alpha magnetic spectrometer, Phys. Rev. Lett. **126**, 081102 (2021).
[27] Xu Pan and Qiang Yuan, Injection spectra of different species of cosmic rays from AMS-02, ACE-CRIS and Voyager-1, Res. Astron. Astrophys. **23**, 115002 (2023).
[28] V. L. Ginzburg and S. I. Syrovatskii, *The Origin of Cosmic Rays* (Pergamon Press, Oxford, 1964).
[29] John Skilling, Cosmic rays in the galaxy: Convection or diffusion?, Astrophys. J. **170**, 265 (1971).
[30] E. N. Parker, The passage of energetic charged particles through interplanetary space, Planet. Space Sci. **13**, 9 (1965).
[31] C. Evoli, D. Gaggero, D. Grasso, and L. Maccione, Cosmic ray nuclei, antiprotons and gamma rays in the galaxy: A new diffusion model, J. Cosmol. Astropart. Phys. 10 (2008) 018.
[32] A. U. Abeysekara, A. Albert, R. Alfaro *et al.*, Extended gamma-ray sources around pulsars constrain the origin of the positron flux at Earth, Science **358**, 911 (2017).
[33] F. Aharonian, Q. An, L. X. Axikegu, Bai *et al.*, Extended very-high-energy gamma-ray emission surrounding PSR J 0622 + 3749 observed by LHAASO-KM2A, Phys. Rev. Lett. **126**, 241103 (2021).
[34] Gary L. Case and Dipen Bhattacharya, A new Σ-D relation and its application to the galactic supernova remnant distribution, Astrophys. J. **504**, 761 (1998).
[35] L. J. Gleeson and W. I. Axford, Solar modulation of galactic cosmic rays, Astrophys. J. **154**, 1011 (1968).
[36] M. Aguilar, L. Ali Cavasonza, B. Alpat *et al.*, Observation of the identical rigidity dependence of He, C, and O cosmic rays at high rigidities by the alpha magnetic spectrometer on the International Space Station, Phys. Rev. Lett. **119**, 251101 (2017).
[37] M. Aguilar, L. Ali Cavasonza, G. Ambrosi *et al.*, Properties of cosmic helium isotopes measured by the alpha magnetic spectrometer, Phys. Rev. Lett. **123**, 181102 (2019).
[38] R. L. Workman, V. D. Burkert, V. Crede *et al.*, Review of particle physics, Prog. Theor. Exp. Phys. **2022**, 083C01 (2022).
[39] A. C. Cummings, E. C. Stone, B. C. Heikkila, N. Lal, W. R. Webber, G. Jóhannesson, I. V. Moskalenko, E. Orlando, and T. A. Porter, Galactic cosmic rays in the local interstellar medium: Voyager 1 observations and model results, Astrophys. J. **831**, 18 (2016).

Correction: The previously published top left panel of Fig. 3 and right panel of Fig. 4 contained errors and have been replaced.